Jonathan P. Cummings

Department of Mechanical and Industrial
Engineering,
University of Massachusetts Amherst,
160 Governors Drive,
Amherst, MA 01003
e-mail: cummij3@gmail.com

Dirk Ruiken

College of Information and Computer Sciences,
University of Massachusetts Amherst,
140 Governors Drive,
Amherst, MA 01003
e-mail: ruiken@cs.umass.edu

Eric L. Wilkinson

College of Information and Computer Sciences,
University of Massachusetts Amherst,
140 Governors Drive,
Amherst, MA 01003
e-mail: ewilkinson@cs.umass.edu

Michael W. Lanighan

College of Information and Computer Sciences,
University of Massachusetts Amherst,
140 Governors Drive,
Amherst, MA 01003
e-mail: lanighan@cs.umass.edu

Roderic A. Grupen

College of Information and Computer Sciences,
University of Massachusetts Amherst,
140 Governors Drive,
Amherst, MA 01003
e-mail: grupen@cs.umass.edu

Frank C. Sup IV[1]

Department of Mechanical and Industrial
Engineering,
University of Massachusetts Amherst,
160 Governors Drive,
Amherst, MA 01003
e-mail: sup@umass.edu

A Compact, Modular Series Elastic Actuator

This paper presents the development of a compact, modular rotary series elastic actuator (SEA) design that can be customized to meet the requirements of a wide range of applications. The concept incorporates flat brushless motors and planetary gearheads instead of expensive harmonic drives and a flat torsional spring design to create a lightweight, low-volume, easily reconfigurable, and relatively high-performance modular SEA for use in active impedance controlled devices. The key innovations include a Hall effect sensor for direct spring displacement measurements that mitigate the negative impact of backlash on SEA control performance. Both torque and impedance controllers are developed and evaluated using a 1-degree-of-freedom (DoF) prototype of the proposed actuator package. The results demonstrate the performance of a stable first-order impedance controller tested over a range of target impedances. Finally, the flexibility of the modular SEA is demonstrated by configuring it for use in five different actuator specifications designed for use in the uBot-7 mobile manipulator requiring spring stiffnesses from $3\,N\cdot m/deg$ to $11.25\,N\cdot m/deg$ and peak torque outputs from $12\,N\cdot m$ to $45\,N\cdot m$.
[DOI: 10.1115/1.4032975]

1 Introduction

Robotic applications that interact with unstructured and partially known environments (especially those with people) often require relatively high torques and low speeds. Further, the use low-latency impedance properties can prevent the robots from damaging themselves and/or the world around them. This design goal places stringent constraints on control and actuation. Moreover, actuator packages must meet this requirement while also minimizing actuator mass and volume, especially at distal joints. SEAs are a popular means of meeting these specifications. SEAs include an elastic element between the motor and the load [1]. This elastic element introduces passive compliance that is independent of control bandwidth. The deflection of these passive elements indicates how contacts with the environment introduce forces on the actuated limb even when these contacts are not predicted a priori. Moreover, distal elasticity filters impact loads on

the robot, protects proximal drivetrains, and provides additional time for active controllers to regulate the impedance of the limb.

The basic design of an SEA includes a motor, spring, and output link. This discussion focuses on the configuration of these components as shown in Fig. 1, where J_m is the rotational moment of inertia of the motor and gearhead, T_m is the motor torque, and θ_m is the motor position. The spring constant and deflection are
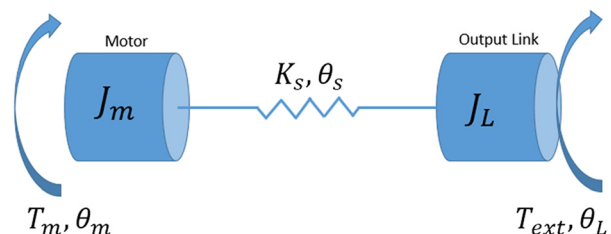

Fig. 1 Schematic of an SEA

---

represented using parameters K_s and θ_s, respectively. The external torque applied to the actuator is T_{ext}, and the position of the link relative to the motor is defined by θ_L.

The deflection of the passive spring element is measured and joint torque is calculated from it using the known spring constant. Torque feedback allows the implementation of a closed-loop impedance (or torque) controller that is used to regulate forces applied anywhere on the load. Often, gearheads require high gear ratios to meet torque/speed specifications in these actuators and they can be damaged by unexpected collisions between the environment and the output link. Passive elasticity and active control based on torque feedback offer protection of the gearhead from such collisions. Moreover, passive compliance provides force feedback and, thus, can be used to improve the force response of an active compliance controller. Compared to rigid actuators, a drawback of SEAs is reduced position control bandwidth. Furthermore, SEAs require additional mechanical components and sensors that raise the cost, complexity, and number of potential failure points in the robot.

Many SEAs in the literature [2–4] use DC motors with large gear reductions that introduce new control challenges associated with friction, backlash, and torque ripple [1]. To minimize these affects, SEAs have been developed that use custom DC motors coupled with low backlash transmissions such as harmonic drive gearheads [2,3,5–8] or ball screws [9,10]. These designs also use either load cells or high-resolution optical position sensors for accurate torque and position measurement. Unfortunately, these approaches use expensive hardware and require highly customized packaging. Other SEA designs have shown that less expensive components such as planetary gearheads can be used to implement stable torque and impedance control [1,11–15].

The contribution of this paper is a modular and SEA design that is relatively lightweight and low volume and can be reconfigured easily to incorporate application-specific motors and springs. In addition, a novel sensor geometry is presented for measuring the deflection of the passive spring directly and minimizing the effect of backlash in planetary gearheads and removing the need for expensive harmonic drives. The result is intended to support robot design by providing a compact, low mass actuator package that addresses a wide range of performance specifications. Modular design considerations can lead to common components and, in volume, to less expensive SEAs and standardized design catalogs for this class of actuator. The paper concludes with a demonstration of how this concept can be applied to a wide range of actuator performance requirements in an integrated, multiple DoF mobile manipulator design that incorporates the modular SEA design.

2 Mechanical Design of a Modular Rotary SEA

The rotary SEA actuator design is shown in Fig. 2. The laboratory prototype incorporates a brushless DC motor (a 70 W Maxon Motors EC 45 Flat) and a planetary gearhead (Maxon Motors GP 32 HP 159:1) that together constitute the J_m component in the system schematic presented in Fig. 1. The configuration of this SEA was chosen such that a designer can consider a standardized actuator package and sensor geometry that is customized for specific applications by selecting: (1) an appropriate spring and (2) an appropriate off-the-shelf motor and planetary gearhead. The compliant element in the SEA is selected from a catalog of planar torsional springs with a linear torque–displacement relationship that can be fabricated using two-dimensional cutting operations. The spring for this SEA package was developed in collaboration with partners at the Johnson Space Center and is similar to a spring design they created for use in the NASA Robonaut 2 platform [2,16].

The output shaft of the gearhead is connected to the torsional spring with a tapered bushing to provide a robust connection between the motor shaft and the spring. Tapered bushings are rated for high joint moments and have zero backlash. The joint is
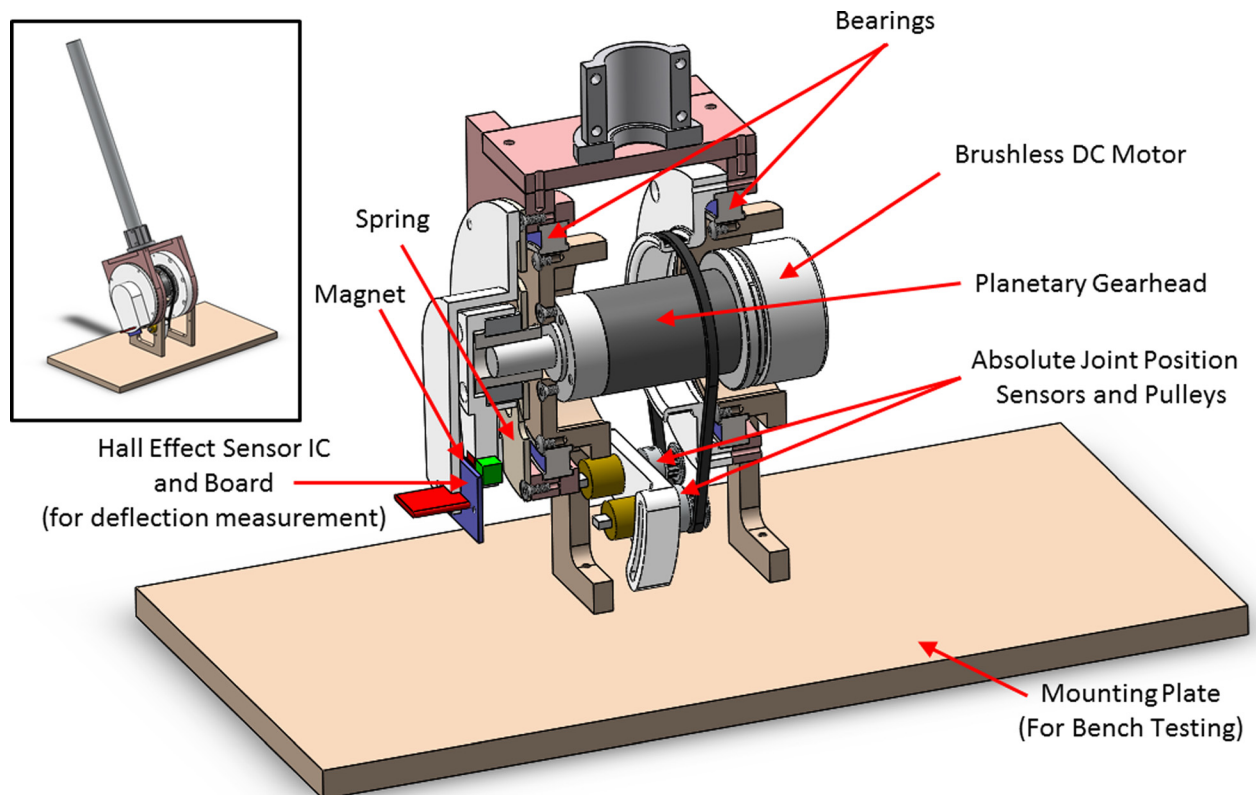

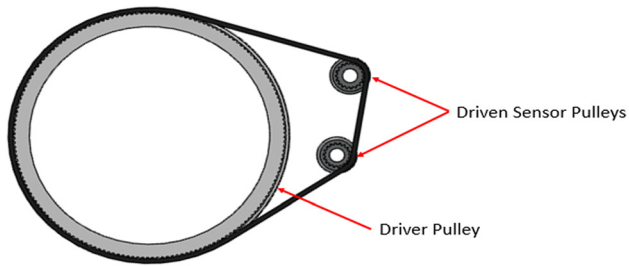
Fig. 2 Cross section view of the prototype SEA joint

Fig. 3 The pulley configuration for a full-range absolute position sensor

Fig. 5 Spring geometry used in SEA [2,16]. The discoloration is a result of the heat treatment process.

supported by two ball bearings to isolate lateral forces acting on the link from the spring and spring deflection sensor.

In a system with backlash, small errors in individual joint positions can accumulate in kinematic chains. Therefore, this actuator measures both motor position and output link position to control output positions accurately (without homing required at start-up) and to compute output loads (using the spring constant of the passive elastic element). To accomplish this, an absolute position sensor is connected to the joint using a belt and pulley as shown in Figs. 2 and 3. The encoders introduce very low loads and are driven by high tensile stiffness, fiberglass reinforced belts to ensure precise measurements in both static and dynamic scenarios. To maintain a desirable form factor, the belt mechanism uses a reduction to decrease the size of the sensor pulley. Therefore, outputs from the encoder are expected to wrap around over the range of motion of the actuator. To address this issue, two sensors driven by the same belt were used with different diameters so that the phase difference encodes joint position. The combination of sensor signals results in a high-resolution encoder that can be designed to measure unique position over the entire joint range of motion. Figure 3 shows an example of the pulley configuration for a joint with a 720 deg range of motion.

A driver pulley with 172 teeth is used to drive two pulleys: one with 18 teeth and the other with 19 teeth. Each sensor pulley is connected to an absolute encoder. Figure 4 shows that by measuring the difference in position between the two-driven pulleys, the position over the entire 720 deg range of motion is measured. The red and green lines indicate the individual position sensors, and the phase difference in blue is proportional to the joint angle
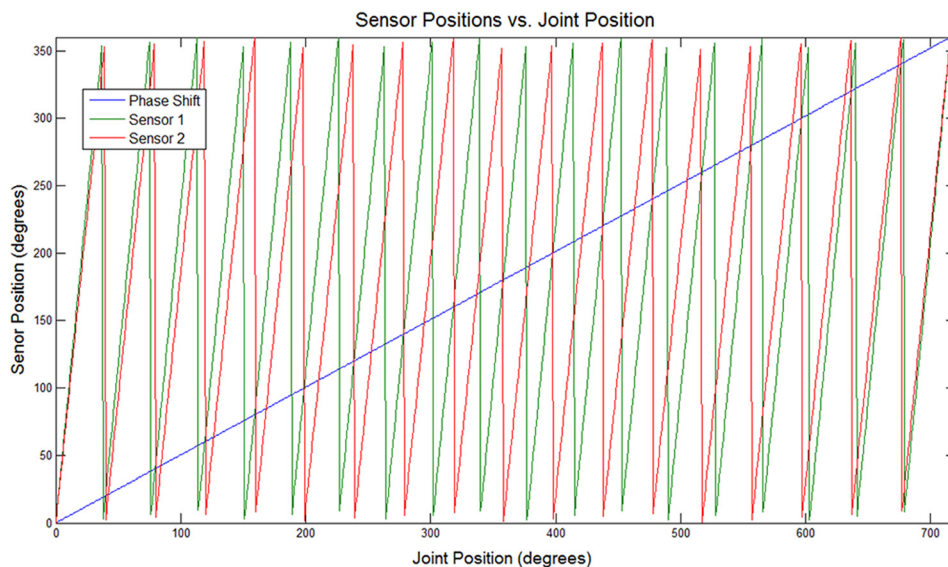
over this range. In this example, the observed phase shift is doubled to obtain the joint position. The precision is better as well; using a pair of 10 bit rotational encoders results in 13-bit precision in the resulting measurement of absolute position.

2.1 Spring Design. An example of the spring geometry proposed is shown in Fig. 5, where the inner bolt circle connects to the gearhead and the outer bolt circle connects to the load. A 17-4PH H900 steel was chosen as the spring material, which has a relatively high yield strain (about four times that of a mild 1018 steel). This is a common material that is available in sheet stock and in low quantities, which helps to lower the cost of material and fabrication. Finite-element analysis and experimental results confirm that the spring constant changes linearly with material thickness for this planar spring geometry. It is a simple matter therefore to replace the spring and to achieve a large range of possible spring constants in a modular design with only minor changes to the package geometry.

The spring constant affects the dynamics of the system, the torque sensing range, resolution, and the speed at which the system can operate safely. Thus, the choice of a proper spring constant is

Fig. 4 Joint sensor positions (repeating sawtooth patterns) and phase shift between the sensors

a critical decision. The methods for correlating the passive compliance to safe operating speeds were discussed in Ref. [17], however, this method is not directly applicable when operating speeds exceed specified limits due to unintentional environmental impact, for example. Other methods for choosing the stiffness parameters in the COMAN humanoid robot [18,19] were explored that focused on the resonant frequencies of the system. Choosing the optimal spring constant for a compliant system is application dependent and remains an open research question.

Neglecting friction and assuming the output of the actuator to be locked, the natural frequency of the system is

$$\omega_n = \sqrt{K_s/J_m} \tag{1}$$

where K_s is the spring constant, and J_m is the motor/gearhead inertia as seen from the input to the spring. Therefore, increasing the spring constant raises the natural frequency of the system and increases the open-loop torque control bandwidth [20]. However, a stiffer spring also reduces the spring deflection and, thus, the torque sensing resolution. Other SEA designs have maximum spring deflections that range from ± 3 deg to ± 50 deg [5,13].

The optimal balance between passive compliance depends on packaging considerations as well as torque sensing resolution and energy storage specifications. Stiff springs provide better torque sensing ranges per unit of angular deflection and, therefore, better torque control bandwidth at the expense of increasing the force transmitted into the gearhead, actuator, and robot. For a given maximum transmitted force, lower spring constants and greater deflections store energy more efficiently and reversibly, but they amplify position errors due to gravity and inertia as well. These errors are exacerbated in multiple DoF kinematic chains. The presented design is a compromise appropriate for applications like the one evaluated in Sec. 4.3 that must exert large control forces—on the same order as the forces that may occur due to falls and unexpected collisions. Furthermore, it is designed to accurately measure contact loads and to support active impedance control.

In the absence of more detailed specifications for the task, a passive compliance was selected based on maximum desired sensed torque and desired torque sensing resolution. For this application, the maximum torque of the motor is used as a maximum desired sensed torque, which happens by design at maximum spring deflection. Therefore, the torque sensing range of the joint covers the full range of motor performance, and closed-loop torque control regulates the full range of actuator torques. To obtain a balance between torque sensing resolution and passive compliance, the maximum deflection range of the spring in the prototype was chosen to be ± 4 deg.

2.2 Spring Deflection Sensing.
The accuracy of the torque controller is dependent on the precision of the spring deflection sensor. Loads can be measured using commercially available load cells as in Ref. [2], however, this approach is expensive and custom load cells require significant development effort. SEAs typically use at least two feedback measurements to calculate joint position and joint torque [3,5–7]. Most of these approaches measure spring deflection to get torque feedback [1,2,9,10,11,13]. Spring deflection can be determined by direct measurements or by differential measurements. A direct measurement of the spring deflection is the most accurate approach. This measurement can be added to motor position (as in Ref. [1]), however, it does not directly measure the joint output position and therefore accumulates additive errors when implemented in kinematic chains. In contrast, differential measurements of the spring deflection are derived from the difference between independent measurements of the joint position and the position of the motor ($\theta_s = \theta_L - \theta_m$) as in Ref. [2]. This works well when there is negligible backlash in the gear train between the sensors, but is subject to additive noise from two differential sensor measurements.

A third method is employed in this work, where both the spring deflection and the output joint position are measured directly as in Refs. [7] and [10]. This approach minimizes position and torque errors, decreases errors due to backlash in the planetary gearheads, and avoids the requirement for a homing routine at start-up. To measure spring deflection, a custom deflection sensor was designed to provide precise measurements over the ± 4 deg deflection range with a 12-bit Hall effect sensor. With a spring deflection of ± 4 deg, a traditional rotary position sensor uses 8 deg out of 360 deg or 2.2% of its operational range—effectively, less than 7 bits of resolution for a 13-bit rotary position sensor.

Figure 6 illustrates a spring deflection sensor that is customized for the ± 4 deg range of spring deflection. The deflection sensor consists of a magnet that is fixed at a radius on a beam that is rigidly connected to the output of the planetary gear. A Hall effect sensor is fixed above the magnet and rigidly connected to the load. For this small deflection, it is assumed that the trajectory of the magnet with respect to the sensor is approximately linear. The arrows in Fig. 7 indicate the trajectory of the sensor relative to a rectangular neodymium magnet. The colors in the plot represent the magnitude of the magnetic flux density, $|B|$. The sensor only measures the Z-component (normal to the surface of the sensor) of the field strength. In Fig. 8, the simulated magnetic flux density in the Z-direction is shown as a function of the offset of the sensor from the center in the Y-direction. The plot verifies that there is an approximately linear relationship between the sensed magnetic field strength and the offset value in millimeters ($R^2 = 0.9995$ over the ± 4.0 mm interval). The simulation was done such that only movement in the Y-direction occurred and no movement in the Z-direction was present. This linear range is specific to the simulated material, and geometry of the magnet and the size of the linear range depend on the distance between the magnet and sensor. The sensor configuration can be modified to work in different scenarios by adjusting the distance between magnet and sensor, changing the beam length or changing the material or geometry of the magnet.

A three-axis Hall effect sensor (Melexis, 90363) was used to validate the simulation. A magnet (K&J Magnetics, B448) was suspended 2.5 mm over the sensor, which was fixed to a micrometer positioning stage. For the first test, the sensor was moved 6 mm across the magnet, and 26 data points were taken. The simulated data are compared to the experimental results in Fig. 8. The experimental data were linear with an R^2 value of 0.9993.

The sensitivity of the magnetic field measurement was evaluated in three static positions, and it was revealed that there is a standard deviation of 5.1 sensor units for 3000 sampled data points. For this setup, 12 bits from the sensor were used and thus the noise corresponds to 0.01 deg. To design the highest resolution deflection sensor, the maximum deflection angle, θ_{max}, was set at ± 4 deg since this sensor configuration is only accurate for small angles. For maximum resolution, the beam length, r, is maximized to increase linear displacement, constrained by the available space within the assembly. The magnet's linear displacement, d, is determined by $d = 2r \sin(\theta_{max})$. In this case, $\theta_{max} = 4$ deg and $r = 35$ mm, and therefore, $d = 5$ mm. The linear region of the magnetic flux density is less than the width of the magnet, and thus, the magnet must be wider than the displacement, d. The polarization of the magnet is oriented parallel to the motion of the sensor as shown in Fig. 7. The strength of the magnet was selected so that it reached the maximum measurable magnetic flux density of the sensor at maximum displacement. It is also important to note that the magnet has sufficient depth (in the X-direction of Fig. 7), so that small perturbations in this direction do not affect the signal.

At the maximum displacement ($d/2$), the magnetic flux density in the Z-direction as a function of air gap size is shown in Fig. 9. Note that for very small air gaps, there is a positive slope. To reach the range in which deflection is linearly proportional to normal magnetic flux density, the air gap must be larger than the value where this peak occurs. The lines intersect at 2.5 mm, and thus, this was the air gap chosen for the prototype design.
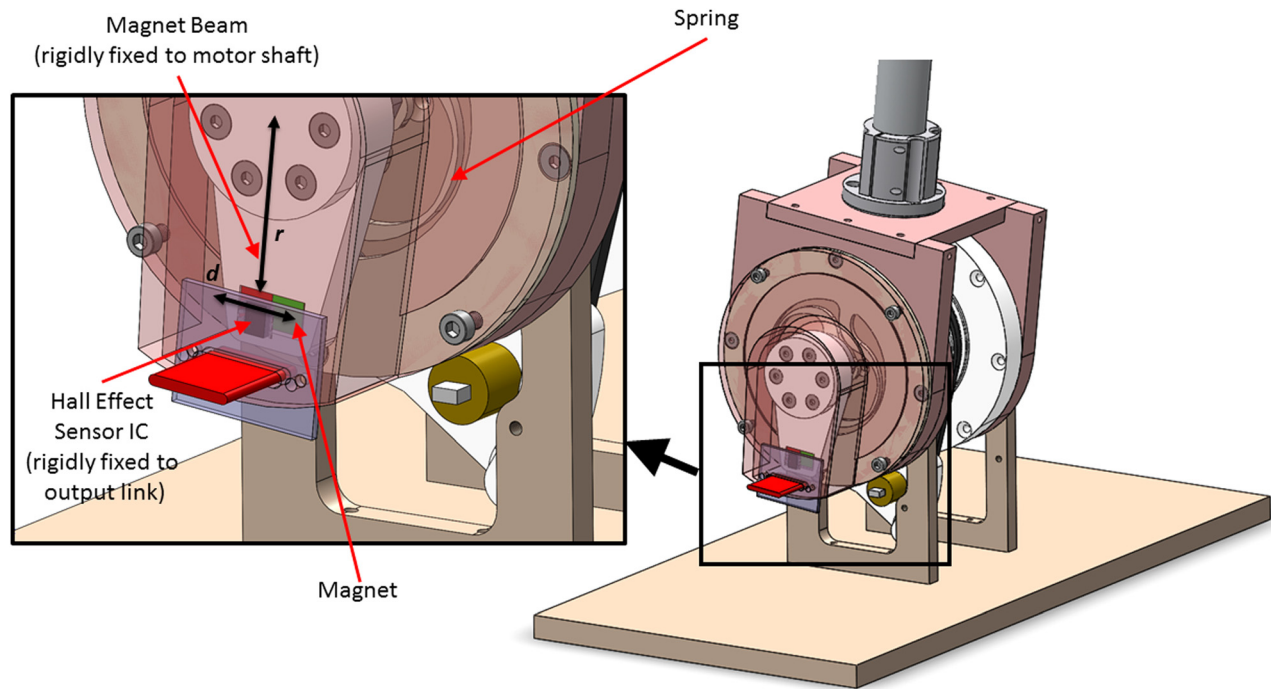
Fig. 6 Spring deflection sensor configuration with beam length, *r*, and linear sensor displacement, *d*, over the deflection range of the spring

3 Controller Design

To determine the equations of motion for the SEA, the output of the joint is locked. This is an approximation of the situation when the manipulator contacts a rigid environment. From the SEA schematic shown in Fig. 10,

$$J_m \ddot{\theta}_m = T_m - K_s \theta_s \qquad (2)$$

$$T_L = K_s \theta_s \qquad (3)$$

$$\theta_m = \theta_L - \theta_s \qquad (4)$$

An impedance controller closes the loop around the net behavior of an embedded torque controller. The proposed SEA is shown in Fig. 11. The impedance control block consists of the transfer function:

$$\frac{T_D(s)}{\theta_e(s)} = K_Z + D_Z s + J_Z s^2 \qquad (5)$$

where T_D is the desired torque resulting from the reference impedance that is the input to a torque controller, θ_e is the difference between desired position θ_D and measured position θ_L, and K_Z, D_Z, and J_Z, are the stiffness, damping, and inertial parameters, respectively, for the desired impedance.

3.1 Torque Controller. The torque controller consists of two major functions: a feedforward component that compensates for
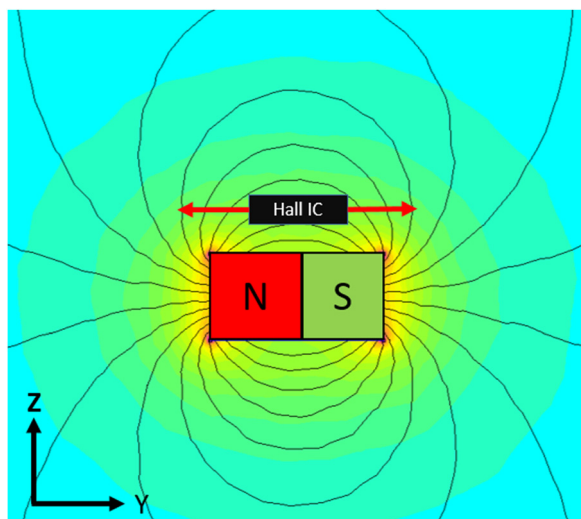

Fig. 7 The sensor movement (indicated by arrows) is shown within the magnet field of a rectangular neodymium magnet. The shading corresponds to the simulated magnitude of the magnetic flux density |*B*| computed using FEMM software [21].
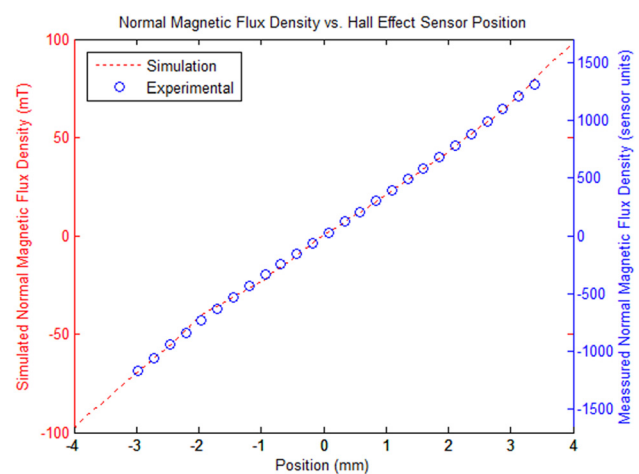

Fig. 8 The normal magnetic flux density versus position from simulation and experimentation on micrometer stage change proportionally to the magnetic field both in simulation and experiment. Simulation and experimental units are different because experimental results did not quantify the actual magnetic field strength.
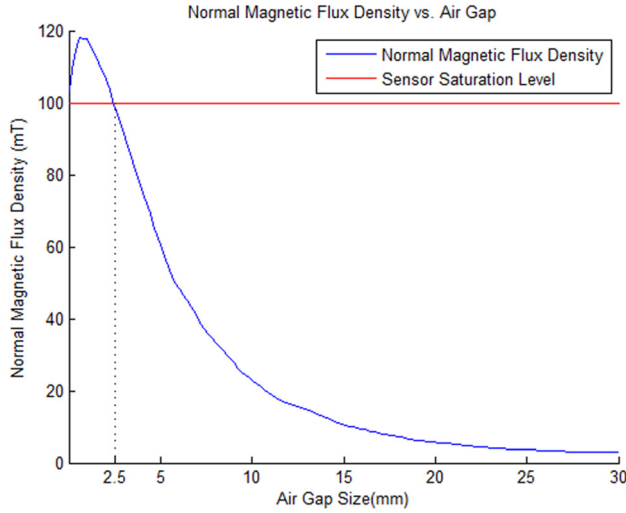
Fig. 9 The magnetic flux density in the Z-direction (normal to surface of the sensor) at maximum displacement (4 mm) is plotted as a function of the size of the air gap

the system dynamics and a PID controller that achieves reference torques. From the motor and spring dynamics (Eqs. (2)–(4)),

$$T_m = T_{LD} + [J_m s^2]\theta_L - [J_m s^2]\theta_s \qquad (6)$$

where T_{LD} is the desired link torque. This equation holds true in the ideal case, however, backlash in the gearhead and noise in sensors can destabilize the feedback control law. To avoid this issue, another position sensor can be used to measure the motor position directly for use in control, yielding

$$T_m = T_{LD} + [K_{Jm} J_m s^2]\theta_m \qquad (7)$$

In Eq. (7), gain $0 \leq K_{Jm} \leq 1$ is used to scale J_m to prevent feedback inversion and instability [1].

The second portion of the torque controller is the feedback portion that reduces errors created from an imperfect model. In this case, a PID controller is used

$$T_m = [T_{LD} - k\theta_s]\left[k_d s + k_p + \frac{k_i}{s}\right] \qquad (8)$$

Combining these controllers (Eqs. (7) and (8)), the following control law is derived:

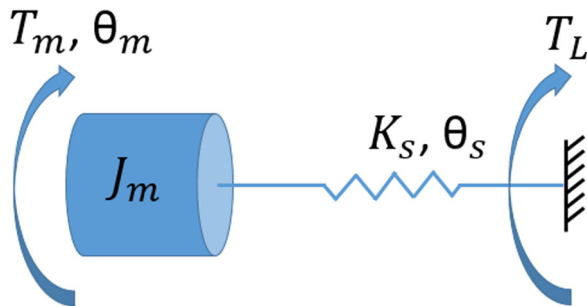$$T_m = T_{LD} + [K_{Jm} J_m s^2]\theta_m + [T_{LD} - k\theta_s]\left[k_d s + k_p + \frac{k_i}{s}\right] \qquad (9)$$

Fig. 10 SEA model used to derive equations of motion assumes that the output link is locked
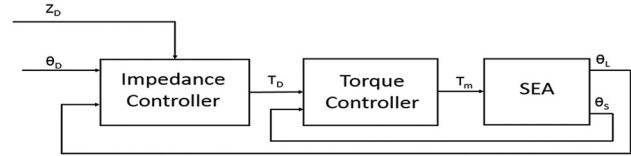
Fig. 11 Joint-level impedance control structure

This is similar to the control law used in Ref. [1], except that the design used in this paper directly measures θ_S.

4 Experiments and Implementation

A prototype SEA (Fig. 2) was implemented using a MicroChip, PIC32MX795F512L microcontroller to process sensor signals and run the impedance and torque control loops. A motor controller (Maxon Motors, ESCON Module 50/5) was used to run closed-loop current control and commutate the motor (Maxon Motors, EC 45 Flat 70 W with a 159:1 planetary gearhead). A $3.6\,\mathrm{N\cdot m}$/deg torsional springlike shown in Fig. 5 was used. The calculated natural frequency of the prototype was $21.2\,\mathrm{rad/s}$.

4.1 Torque Controller Evaluation. To implement the torque controller shown in Eq. (9), the spring deflection and motor position must be measured. In the SEA prototype, motor velocity is measured using the motor commutation Hall effect sensors. This signal is supplied to the motor controller, however, it is too noisy to be accurately differentiated to get acceleration at the controller frequency of 1 kHz and therefore was not used to compensate for motor inertia. For this reason, the following torque control law was implemented with gains of $K_p = 5.0$ and $K_i = 0.002$:

$$T_m = T_{LD} + [T_{LD} - k_s \theta_s]\left[K_p + \frac{K_i}{s}\right] \qquad (10)$$

The frequency response of this controller was tested on the hardware SEA prototype. The results of these tests are illustrated in Fig. 12 where the input signal is a sine wave of amplitude of 1.0, 2.0, and $4.0\,\mathrm{N\cdot m}$ and the output of the joint is locked. An open-loop controller is also plotted to provide a baseline for comparison. The bandwidth of this controlled system is between 20 and $30\,\mathrm{rad/s}$.
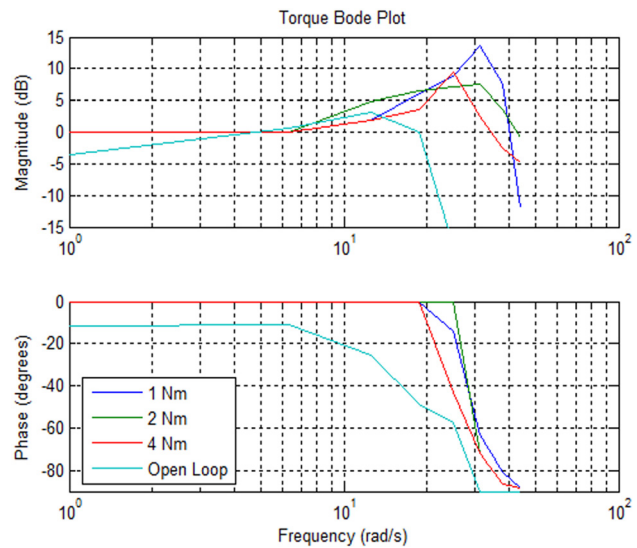

Fig. 12 Bode plot of SEA prototype for sinusoidal torque inputs at three magnitudes ($1.0\,\mathrm{N\cdot m}$, $2.0\,\mathrm{N\cdot m}$, and $4.0\,\mathrm{N\cdot m}$) and the open-loop response
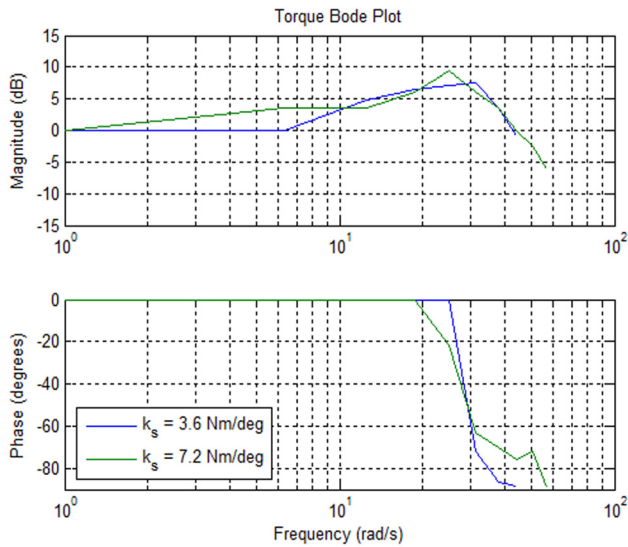
Fig. 13 Torque Bode plot of SEA prototype with spring constants of 3.6 N · m/deg and 7.2 N · m/deg

Fig. 14 Bode plot of actuator torque with 1.0 N · m magnitude sine wave centered at zero causing backlash and centered at 5.0 N · m in order to eliminate backlash

Increasing the system's natural frequency raises the open-loop control bandwidth. To test if this would increase the closed-loop torque control bandwidth, a new spring was fabricated with a doubled spring constant of 7.2 N · m/deg. Figure 13 presents the frequency response of this design using a sine wave with a 2.0 N · m amplitude. Comparing Figs. 12 and 13 reveals that the cutoff frequencies are close for these two conditions. This shows that even though increasing the spring constant increases the system's natural frequency, it does not, in fact, increase the closed-loop bandwidth for this system. This is likely due to the fact that sensor noise and system nonlinearities all remain constant. Also, at higher spring constants torque sensing resolution decreases. Moreover, it was observed that, at higher frequencies, the backlash in the gearhead causes nonlinear and unpredictable behavior. This is partly due to the torque response of the motor without inertial and frictional compensation. At high frequencies, the motor leaves the backlash region only a fraction of the time.

To test what effects backlash has on the system, the frequency response was generated in an operating condition where backlash was not present for comparison. This was accomplished using a
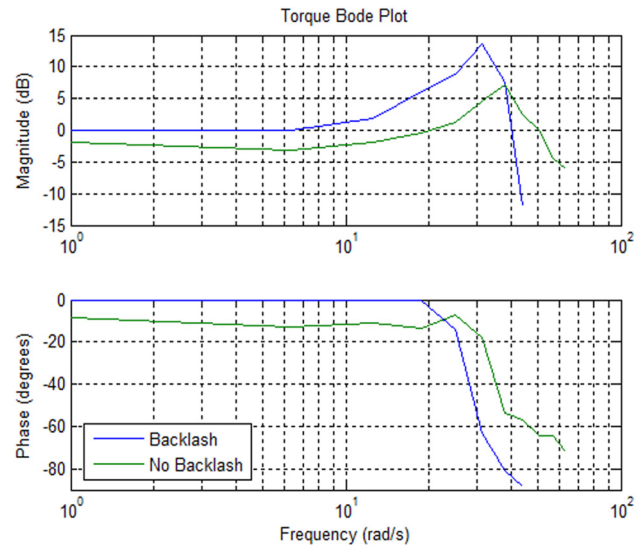
torque sine wave that was offset such that no zero crossing occurred in the input signal. This kept the system torque in one direction and thus remained out of the backlash zone. For this test, a 3.6 N · m/deg spring was used and a sine wave with a 1.0 N · m amplitude with a 5 N · m offset. The results are shown in Fig. 14. In this case, the bandwidth increased from approximately 20 rad/s to 25 rad/s and the system has a lower peak magnitude at resonance. These diagrams also portray a slight phase shift and negative magnitude gain at low frequencies. This can be attributed to friction and stiction, which increase with torque. Bounded by stability margins, the actuator bandwidth can be improved by using higher resolution motor velocity and acceleration feedback and/or by using larger feedback gains.

4.2 Impedance Controller Evaluation. Under impedance control, the impedance parameter, K_z, proved to be controllable in the range from 18 mN · m/deg to 360 mN · m/deg or 1/200th to 1/10th of the physical spring constant. Higher stiffnesses were observed to be unstable. In order to determine the damping

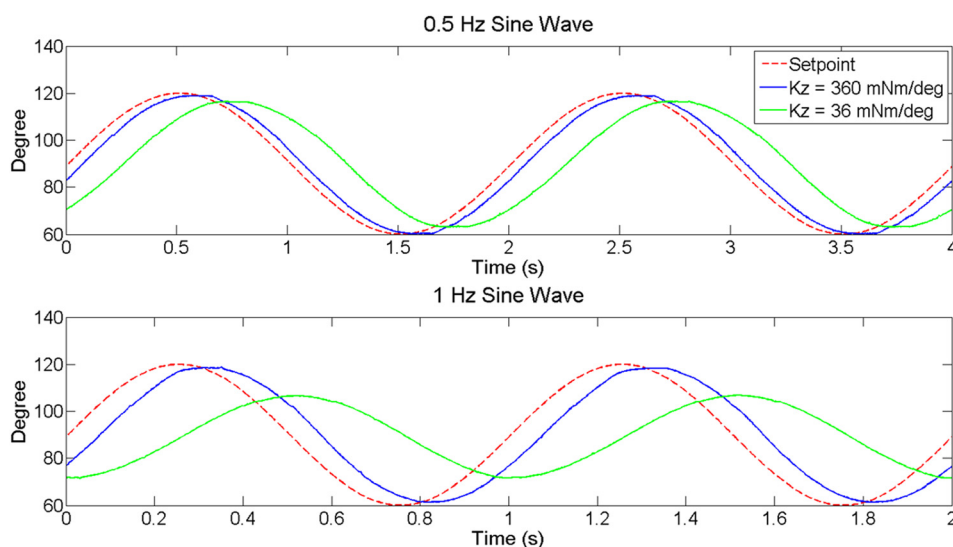**Fig. 15 Trajectory following at 0.5 Hz (top) and 1.0 Hz (bottom) with high impedance ($K_Z = 360$ mN · m/deg and $D_Z = 28.1$ mN · m s/deg) and low impedance ($K_Z = 36$ mN · m/deg and $D_z = 7.3$ mNm s/deg)**

Fig. 16 The SEA prototype with a low impedance setting causes the link to be obstructed (left). Increasing the control impedance overcomes the obstruction (right), shown after the object has been moved and the arm retracted.

Fig. 18 Step response of the impedance controller to a 30 deg step in the vertical plane against gravity at low (36 mN · m/deg) and medium (180 mN · m/deg) stiffnesses

parameter across this range of stiffness values, a quadratic polynomial is used to fit K_z and D_z pairs in this range that resulted in critically damped step responses. Unless otherwise stated, the following equation was used to determine D_z values in all the following experiments:

$$D_z = 0.0028 + \frac{0.474 K_z}{K_s} + 2.211 \left(\frac{K_z}{K_s}\right)^2 \qquad (11)$$

The inertial parameter, J_Z, was not implemented due to lack of resolution in acceleration measurement. Figure 15 shows the system response to sine wave position trajectories of 0.5 Hz and 1.0 Hz frequency. The response was evaluated for two stiffnesses: $K_Z = 360$ mN · m/deg (high) and $K_Z = 36$ mN · m/deg (low). The damping parameter, D_Z, was calculated using Eq. (11). At 0.5 Hz, the high impedance controller follows the trajectory more closely than the low impedance controller as expected. Furthermore, the low impedance mode has comparatively more magnitude error and phase lag. However, at 1 Hz both impedances show deviations from the desired trajectory. The higher stiffness results in more precise position control at the cost of higher contact forces in the event of contact.

The impedance controller's response upon contact was evaluated by placing a 2.0 kg calibrated weight in arm's trajectory as shown in Fig. 16. The desired position trajectory was a 0.25 Hz sine wave oscillating between 60 deg and 120 deg. The results presented in Fig. 17 show the measured and desired positions and torques. At approximately 5 s, the joint makes contact with the obstacle. For the high impedance controller ($K_Z = 360$ mN · m/deg), there is a slight deviation from the desired trajectory and a peak torque of 4 N · m is observed. The calibrated mass is pushed

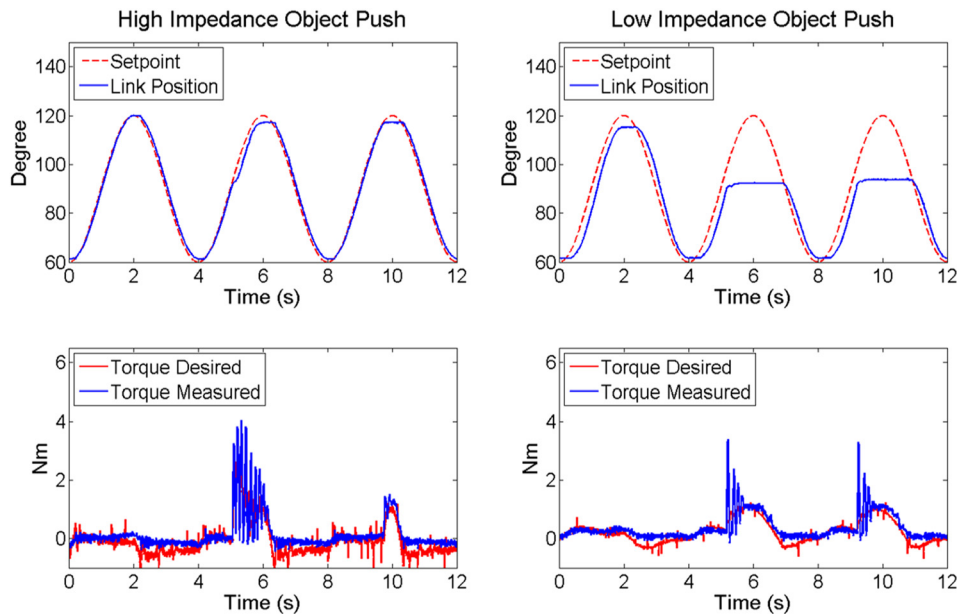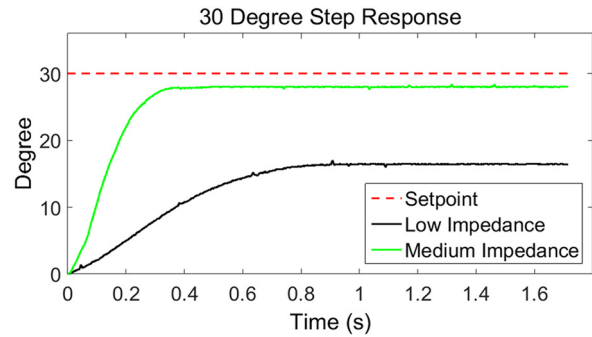almost completely to the edge of the sine wave trajectory. This same test was done with lower impedance ($K_Z = 36$ mN · m/deg). Due to the low impedance parameters, the desired torque remains low (1.3 N · m) even under large position errors. The desired torque is proportional to the difference between the desired and actual position and velocity.

A spectrogram of the desired torque commands revealed that a great deal of energy is distributed more or less uniformly over time and frequency. It appears to be constant before and after impact and is proportional to impedance setpoints. We, therefore, conclude that this is the effect of noise in the velocity estimation. The vast majority of this energy is at frequencies significantly greater than the bandwidth of the torque controller, so it was not necessary to filter the high-frequency components of the desired torque before submitting it to the torque controller.

The next experiment evaluated the actuator's response to a step position command under impedance control. The results are shown in Fig. 18 for two different stiffnesses where the impedance controlled actuator was subjected to a 30 deg step error in a vertical plane. The low and medium stiffnesses (K_Z) used in this case were 36 mN · m/deg and 180 mN · m/deg and with damping values (D_Z) determined by the fitting function Eq. (10). In this case, the experiment was conducted in a configuration where movement is against gravity. As a result, the low stiffness controller exhibits an approximately 15 deg steady-state error and the
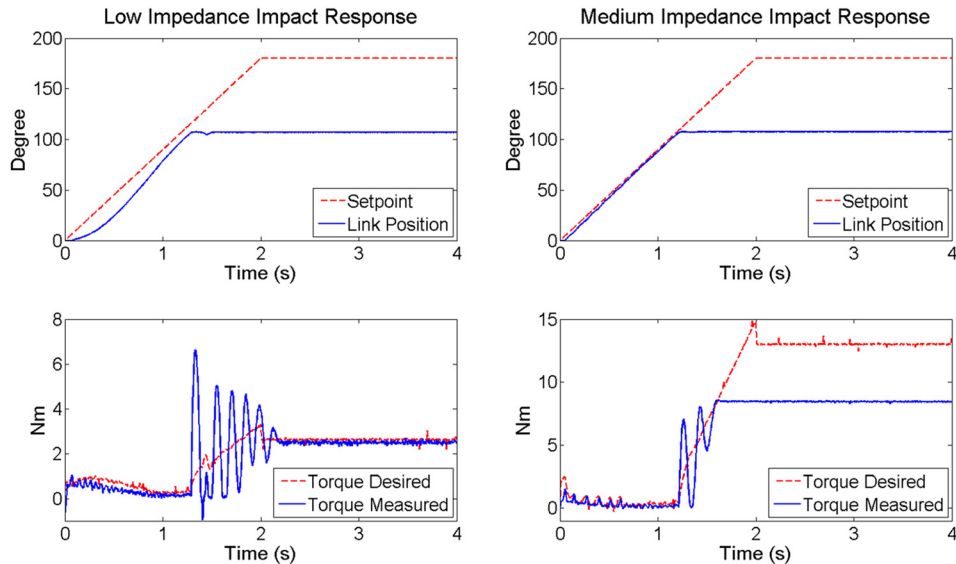

Fig. 17 A 0.25 Hz reference trajectory with $K_z = 360$ mN · m/deg and $D_z = 28.1$ mN · m s/deg (left) and $K_z = 36$ mN · m/deg and $D_z = 7.3$ mNm s/deg with a collision at approximately 5 s

Fig. 19 The impact response of the impedance controller at medium and low stiffnesses, 180 mN · m/deg and 36 mN · m/deg. The link encounters a fixed metal rod at approximately 110 deg. Note that the gap between measured and desired torque for the medium impedance case is due to the limitations on current drawn from the motor.

medium stiffness controller shows approximately 2 deg of steady-state error.

Finally, an experiment was designed to evaluate the compliance of the SEA design in case of impact with a rigid body. The link was commanded to follow a linear trajectory of 90 deg/s through joint space before encountering a fixed metal rod placed at approximately 110 deg. The results are shown in Fig. 19 for low and medium stiffnesses, where the impedance controlled actuator displays a resonance response while tracking the desired torque. The ringing effect at impact with the rigid obstruction likely comes from the natural frequency of the prototype system (21.2 rad/s) and is not included in the torque controller due to the absence of motor position information.

4.3 Implementation: uBot-7. We evaluate the contention that this modular design can accommodate a large variety of actuator design specifications without significant redesign. This section applies the modular SEA to multiple design conditions present in a single mobile manipulation concept. The uBot platform, developed at the University of Massachusetts Amherst, Amherst, MA, was chosen for this analysis because it is designed to be a lightweight, low-cost, high-performance platform that introduces a large range of actuator design parameters. Also, the uBot is a balancing mobile manipulator that is subject to forces from inadvertent falls and other (controlled and uncontrolled) collisions with the environment. Previous generations of uBots have made significant contributions in the areas of dexterous mobility [22–24], emergency response [25], and physical rehabilitation [26–29]. To develop new capabilities and to operate safely and effectively in dynamic and human-centered environments, torque sensing capabilities are required that support compliant interaction with the environment and haptic exploration. To expand the
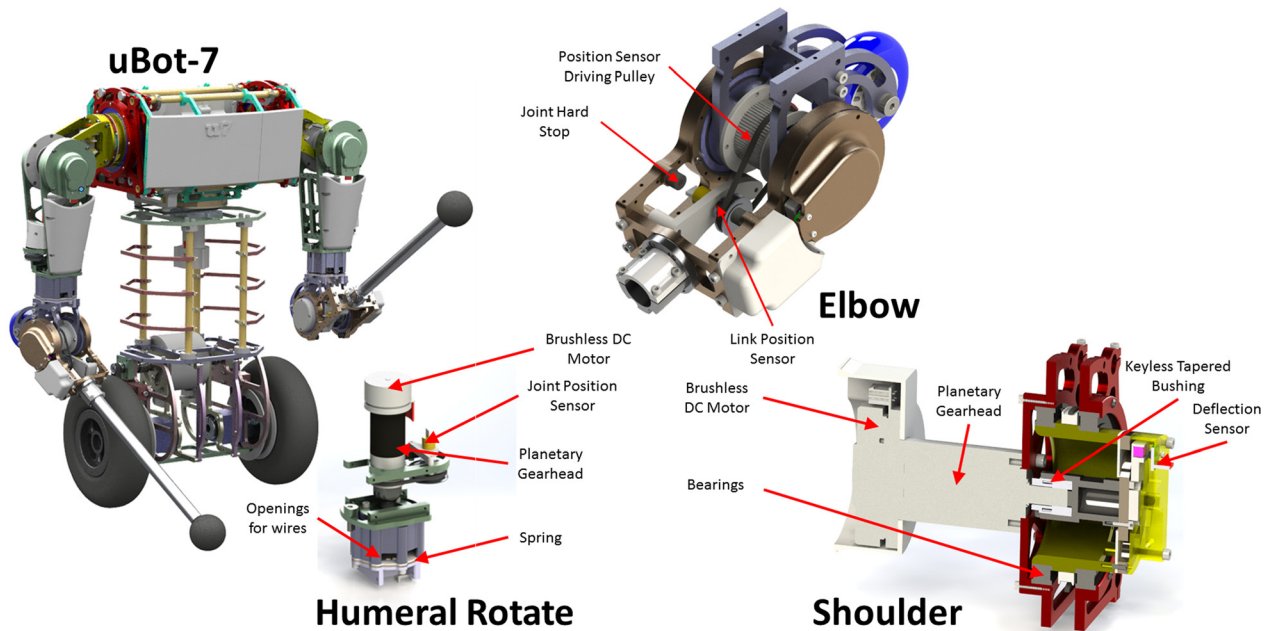

Fig. 20 uBot-7 SEA joints in shoulder flexion/extension, elbow flexion/extension abduction/adduction, and humeral rotate

Table 1 uBot-7 joint maximum torque and no load speed compared to the values determined from functional requirements

	Torque (N·m)	No load speed (rpm)	Motor (power)	Planetary gearhead (reduction)
Torso	12	39	Maxon EC 45 Flat (70 W)	Maxon GP 32 HP (159:1)
Shoulder flexion	45	19	Maxon EC 90 Flat (90 W)	Maxon GP 52 C (113:1)
Shoulder abduction	21	27	Maxon EC 45 Flat (70 W)	Maxon GP 42 C (230:1)
Shoulder twist	12	39	Maxon EC 45 Flat (70 W)	Maxon GP 32 HP (159:1)
Elbow	12	39	Maxon EC 45 Flat (70 W)	Maxon GP 32 HP (159:1)

Table 2 uBot-7 SEA joint natural frequencies

	Spring constant (N·m/deg)	Motor inertia (g cm^2)	Reduction (N:1)	Natural frequency (rad/s)
Torso	3	181	159	19.39
Shoulder flexion	11.25	3060	113	12.85
Shoulder abduction	5.25	181	260	15.68
Shoulder twist	3	181	159	19.39
Elbow	3	181	159	19.39

sensing capabilities of the uBot and enable safe human–robot interaction, the latest iteration, uBot-7, has been designed to include the modular SEA joints developed in this paper in its nine primary joints (2-DoF shoulder, humeral rotation, elbow for two arms, and torso twist). The uBot-7 design is shown in Fig. 20 along with three of the five independent SEA configurations for shoulder, elbow, and humeral rotation axes.

The uBot series of robots balance on a differentially steered, two-wheeled platform and may fall, in which case, impact loads on the arms may exceed normal design loads. These conditions can produce forces that damage gearheads unless filtered by the passive properties of the SEA. This potential for failure is a central motivation for considering SEAs in these kinds of applications.

The actuator torque and speed requirements for uBot-7 were developed in Ref. [30]. These requirements are based on experience with uBot-5 and 6 and provide adequate torque for supporting upright and prone postural modes presented in Ref. [23]. The planetary gearheads used in previous uBots have about 1 deg of backlash. Higher performance reductions with less backlash are available, but are much more expensive. However, it has been shown that planetary gearheads can be applied in high bandwidth control applications [15], bandwidths that are adequate for impedance control [8]. Based on these findings, less expensive gearheads like those used previously in uBot-5 and 6 were selected. Table 1 shows the maximum torque and no load speed for each joint determined from the manufacturer's specifications. A detailed discussion of the design of each joints designed for the uBot-7 is presented in Ref. [30].

The spring constant chosen for each joint used the same method as in Sec. 2.2 of this paper: maximum motor torque divided by maximum spring deflection (4 deg in this case). Using Eq. (1) and assuming the output of the joint is locked, the natural frequency for each joint can be calculated and the results are reported for uBot-7 in Table 2. Even though the actuators have different spring constants and motor inertias, the natural frequencies are all between 10 and 20 rad/s.

5 Conclusions

This paper presents an SEA design consisting of standard brushless DC motors and planetary gearheads. The linear springs used in the actuator feature a planar geometry that can be easily manufactured and reconfigured to attain a wide variety of spring constants. The sensors chosen to deliver position and force tracking control are precise, measure spring deflection directly, are designed to be low-cost, and contribute to a desirable form factor. Spring deflection is measured directly using a customized Hall effect sensor combination to mitigate the effects of backlash, and

joint position is measured over large ranges of motion using a phase-shifted pair of encoders. Torque and impedance controllers are developed and tested on a 1-DoF prototype. The impedance controller can be implemented with any torque controller and therefore can be easily extended to other applications. The torque controller proved that stable torque control can be implemented up to input frequencies of 25 rad/s. Using the presented torque control law, a range of stiffnesses was implemented in the controlled dynamical system ranging from $18\,\mathrm{mN}\cdot\mathrm{m/deg}$ to $360\,\mathrm{mN}\cdot\mathrm{m/deg}$ (1/200th to 1/10th of the physical spring constant). Trajectory tracking, collision, and step response results were presented for this impedance controller with a range of virtual stiffnesses. The new SEA actuator design was applied in five different joint configurations with varying torque requirements in a mobile robot. This illustrates the range of applicability for the SEA concept for torque feedback over a significant variation in design specifications. In future work, we will evaluate the adequacy of the multi-DoF impedance design. The flexibility of the modular SEA design will make tuning these parameters a simple exercise, potentially only involving a spring replacement.

Nomenclature

B = magnetic flux density
d = linear displacement of magnet
D_z = virtual damping parameter
J_L = load inertia
J_m = effective motor inertia after reduction
J_z = virtual inertia parameter
k_p, k_i, k_d = PID controller gains
K_s = spring constant
K_z = virtual spring parameter
K_{Jm} = inertia scaling factor
N = transmission ratio
r = magnet beam length
T_D = desired torque calculated by the impedance controller
T_l = link torque
T_m = motor torque
T_{ext} = external torque on actuator
T_{LD} = desired link torque
θ_D = desired position
θ_e = deviation from the desired position
θ_L = measured output link angle
θ_m = measured motor position
θ_S = measured spring angle
θ_{max} = maximum deflection angle of Hall effect sensor
ω_n = natural frequency

References

[1] Pratt, G., and Williamson, M., 1995, "Series Elastic Actuators," IEEE/RSJ Int. Conf. Intell. Robot. Syst., **1**(1524), pp. 399–406.

[2] Diftler, M. A., Mehling, J. S., Abdallah, M. E., Radford, N. A., Bridgwater, L. B., Sanders, A. M., Askew, R. S., Linn, D. M., Yamokoski, J. D., Permenter, F. A., Hargrave, B. K., Platt, R., Savely, R. T., and Ambrose, R. O., 2011, "Robonaut 2: The First Humanoid Robot in Space," IEEE International Conference on Robotics and Automation, Shanghai, China, May 9–13, pp. 2178–2183.

[3] Tsagarakis, N. G., Saglia, J., and Caldwell, D. G., 2011, "The Design of the Lower Body of the Compliant Humanoid Robot 'cCub'," IEEE International Conference on Robotics and Automation, Shanghai, China, May 9–13, pp. 2035–2040.

[4] Tsagarakis, N. G., Morfey, S., Medrano Cerda, G., Zhibin, L., and Caldwell, D. G., 2013, "Compliant Humanoid Coman: Optimal Joint Stiffness Tuning for Modal Frequency Control," IEEE International Conference on Robotics and Automation, Karlsruhe, Germany, May 6–10, pp. 673–678.

[5] Tsagarakis, N. G., Laffranchi, M., Vanderborght, B., and Caldwell, D. G., 2009, "A Compact Soft Actuator Unit for Small Scale Human Friendly Robots," IEEE International Conference on Robotics and Automation, Kobe, Japan, May 12–17, pp. 4356–4362.

[6] Tsagarakis, N. G., Vanderborght, B., Laffranchi, M., and Caldwell, D. G., 2009, "The Mechanical Design of the New Lower Body for the Child Humanoid Robot 'iCub'," IEEE/RSJ International Conference on Intelligent Robots and System, St. Louis, MO, Oct. 11–15, pp. 4962–4968.

[7] Lagoda, C., Schouten, A. C., Stienen, A. H. A., Hekman, E. E. G., and Van Der Kooij, H., 2010, "Design of an Electric Series Elastic Actuated Joint for Robotic Gait Rehabilitation Training," IEEE RAS and EMBS International Conference on Biomedical Robotics and Biomechatronics, Tokyo, Japan, Sept. 26–29, pp. 21–26.

[8] Sergi, F., Accoto, D., Carpino, G., Tagliamonte, N. L., and Guglielmelli, E., 2012, "Design and Characterization of a Compact Rotary Series Elastic Actuator for Knee Assistance During Overground Walking," IEEE RAS and EMBS International Conference on Biomedical Robotics and Biomechatronics, Rome, Italy, June 24–27, pp. 1931–1936.

[9] Paine, N., Oh, S., and Sentis, L., 2014, "Design and Control Considerations for High-Performance Series Elastic Actuators," IEEE/ASME Trans. Mechatronics, 19(3), pp. 1080–1091.

[10] Wang, S., Meijneke, C., and van der Kooij, H., 2013, "Modeling, Design, and Optimization of Mindwalker Series Elastic Joint," IEEE International Conference on Rehabilitation Robotics, Seattle, WA, June 24–26, p. 6650381.

[11] Wyeth, G., 2006, "Control Issues for Velocity Sourced Series Elastic Actuators," Proceedings of the Australasian Conference on Robotics and Automation, B. MacDonald, ed., Australian Robotics and Automation Association Inc, Auckland, New Zealand, Paper No. 32843.

[12] Thorson, I., and Caldwell, D., 2011, "A Nonlinear Series Elastic Actuator for Highly Dynamic Motions," IEEE/RSJ International Conference on Intelligent Robots and System, San Francisco, CA, Sept. 25–30, pp. 390–394.

[13] Kong, K., Bae, J., Member, S., and Tomizuka, M., 2012, "A Compact Rotary Series Elastic Actuator for Human Assistive Systems," IEEE/ASME Trans. Mechatronics, 17(2), pp. 288–297.

[14] Kong, K., Bae, J., and Tomizuka, M., 2009, "Control of Rotary Series Elastic Actuator for Ideal Force-Mode Actuation in Human–Robot Interaction Applications," IEEE/ASME Trans. Mechatronics, 14(1), pp. 105–118.

[15] Sensinger, J., and Weir, R., 2006, "Improvements to Series Elastic Actuators," IEEE/ASME International Conference on Mechatronics and Embedded Systems and Application, Beijing, China, Aug., pp. 1–7.

[16] Ihrke, C., Mehling, J., Parsons, A. H., Grif, B. K., Radford, N. A., Permenter, F. N., Davis, D. R., and Ambrose, R. O., 2012, "Rotary Series Elastic Actuator," U.S. Patent No. 8291788 B2.

[17] Bicci, A., and Tonietti, G., 2004, "Fast and 'Soft-Arm' Tactics," IEEE Robot. Autom. Mag., 11(2), pp. 22–33.

[18] Li, Z., Vanderborght, B., Tsagarakis, N. G., Colasanto, L., and Caldwell, D. G., 2012, "Stabilization for the Compliant Humanoid Robot COMAN Exploiting Intrinsic and Controlled Compliance," IEEE International Conference on Robotics and Automation, St. Paul, MN, May 14–18, pp. 2000–2006.

[19] Moro, F. L., Tsagarakis, N. G., and Caldwell, D. G., 2011, "A Human-Like Walking for the Compliant Humanoid COMAN Based on CoM Trajectory Reconstruction From Kinematic Motion Primitives," 11th IEEE-RAS International Conference on Humanoid Robots, Bled, Slovenia, Oct. 26–28, pp. 364–370.

[20] Robinson, D. W., Pratt, J. E., Paluska, D. J., and Pratt, G. A., 1999, "Series Elastic Actuator Development for a Biometric Walking Robot," IEEE/ASME International Conference on Advanced Intelligent Mechatronics, Atlanta, GA, pp. 561–568.

[21] 2013, "Finite Element Method Magnetics," Last accessed Apr. 6, 2015, http://www.femm.info/wiki/HomePage

[22] Kuindersma, S. R., Hannigan, E., Ruiken, D., and Grupen, R. A., 2009, "Dexterous Mobility With the uBot-5 Mobile Manipulator," 14th International Conference on Advanced Robotics, Munich, Germany, June 22–26, pp. 1–7.

[23] Ruiken, D., Lanighan, M. W., and Grupen, R. A., 2013, "Postural Modes and Control for Dexterous Mobile Manipulation: The UMass uBot Concept," 13th IEEE-RAS International Conference on Humanoid Robots, Atlanta, GA, Oct. 15–17, pp. 280–285.

[24] Ruiken, D., Lanighan, M. W., and Grupen, R. A., 2014, "Path Planning for Dexterous Mobility," 24th International Conference Automated Planning and Schedules, pp. 1–5.

[25] Jung, H., Takahashi, T., and Grupen, R., 2014, "Human-Robot Emergency Response: Experimental Platform and Preliminary Dataset," Technical Report No. UM-CS-2014-006.

[26] Jung, H., Choe, Y., Baird, J., and Grupen, R., 2012, "A Follow-Up on Humanoid-Mediated Stroke Physical Rehabilitation," Seventh Annual ACM/IEEE International Conference on Human-Robot Interaction, pp. 159–160.

[27] Choe, Y., Jung, H., Baird, J., and Grupen, R., 2013, "Multidisciplinary Stroke Rehabilitation Delivered by a Humanoid Robot: Interaction Between Speech and Physical Therapies," Aphasiology, 27(3), pp. 252–270.

[28] Jung, H., Baird, J., Choe, Y., and Grupen, R., 2011, "Upper Extremity Physical Therapy for Stroke Patients Using a General Purpose Robot," IEEE RO-MAN, Atlanta, GA, July 31–Aug. 3, pp. 270–275.

[29] Jung, H.-T., Takahashi, T., Choe, Y.-K., Baird, J., Foster, T., and Grupen, R. A., 2013, "Towards Extended Virtual Presence of the Therapist in Stroke Rehabilitation," IEEE International Conference on Rehabilitation Robotics, Seattle, WA, June 24–26, pp. 1–6.

[30] Cummings, J., 2014, "uBot-7: The Design of a Compliant Dexterous Mobile Manipulator," Master thesis, University of Massachusetts Amherst, Amherst, MA.